Composites Part A 121 (2019) 499–509

Contents lists available at ScienceDirect

Composites Part A

journal homepage: www.elsevier.com/locate/compositesa

Considering the stress concentration of fiber surfaces in the prediction of the tensile strength of unidirectional carbon fiber-reinforced plastic composites

Go Yamamoto[a,*], Miho Onodera[a], Keita Koizumi[a], Jun Watanabe[b], Haruki Okuda[b], Fumihiko Tanaka[b], Tomonaga Okabe[a,c]

[a] Department of Aerospace Engineering, Tohoku University, 6-6-01 Aramaki-Aza-Aoba, Aoba-ku, Sendai 980-8579, Japan
[b] Composite Material Research Laboratories (CMRL), Toray Industries, Inc., 1515, Tsutsui, Masaki-cho, Iyogun, Ehime 791-3193, Japan
[c] Department of Materials Science and Engineering, University of Washington, Seattle, WA 98195, USA

ARTICLE INFO

Keywords:
A. Polymer-matrix composites (PMCs)
B. Fragmentation
B. Strength
B. Stress concentrations

ABSTRACT

The tensile strengths of unidirectional carbon fiber-reinforced plastic (CFRP) were predicted by using a spring element model that considers the surface stress concentration on fibers caused by a fracture site in an adjacent fiber. The surface stress concentration on the fibers was experimentally evaluated by implementing multi-fiber fragmentation tests in conjunction with a spring element model simulation. Four types of epoxy materials were utilized to explore the effects of matrix polymer properties on the surface stress concentration of the fibers. The size scaling results, coupled with the results of the spring element model simulation, designed to take into account the surface stress concentration, were reasonably consistent with the experimental data on the tensile strengths of the unidirectional CFRP composites, regardless of the differences in the matrix mechanical properties. Possible mechanisms by which additional stress concentration is generated on an intact fiber surface were analyzed numerically using the finite element method.

1. Introduction

Composite materials are attracting the attention of people within the engineering sector because of their unique mechanical properties and ease of property customization, making them highly competitive with conventional materials. Carbon fiber reinforced plastic (CFRP), a common class of composite materials, is increasingly being used as a lightweight and high-stiffness material in various applications. The process of determining the potential amount of weight that can be saved requires that the fracture properties of the CFRPs in the direction of the fiber axis be a major consideration in the design of composite structures. Thus, improving the accuracy of tensile strength prediction methods continues to be central to CFRP composite research.

Since the early pioneering work by Cox [1], Rosen [2], and Kelly et al. [3], a number of models have been proposed to predict the tensile strength of unidirectional CFRP composites. The work of Hedgepeth and Van Dyke became the original report on failure process modeling of unidirectional fiber reinforced composites (UD composites) [4]. They implemented a discrete Fourier transform to analytically describe the redistribution of load resulting from fiber breakage in a hexagonal fiber array. Subsequently, Suemasu [5,6] showed that such redistribution can be derived by employing a method based on Green's functions. By contrast, Rosen [2] focused on the role of the matrix in determining the stress transfer length around fiber break points, although without considering the in-plane stress concentration in strength analysis. Zweben [7] later introduced the stress concentration effect caused by fiber breaks into Rosen's model [2]. Although the effects of both in-plane stress concentration and the stress recovery of broken fibers are expected to require an accurate failure process prediction, further research is needed to establish an appropriate analytical approach. Furthermore, instead of focusing on correcting this oversight, many researchers have opted to focus on simulating the failure processes of multiple types of UD composites comprising various matrix materials by utilizing a procedure that implements a phantom step to solve the 2D shear-lag equation [8–11]. Additionally, Sastry et al. [12] and Beyerlein et al. [13] proposed a sophisticated approach, referred to as the break-influence superposition (BIS) technique and extended it to develop the quadratic influence superposition (QIS) technique within the framework of a 2D model. However, the stress concentration of a 2D model is well known to be significantly higher than that of the corresponding 3D model. Zhou and Curtin [14] proposed a novel numerical simulation based on the lattice Green function (LGF) approach to analyze the 3D stress state of the composites. Building on their work, Landis et al. [15] and Okabe et al. [16] attempted to develop the 2D shear-lag model into

* Corresponding author.
E-mail address: yamamoto@plum.mech.tohoku.ac.jp (G. Yamamoto).

https://doi.org/10.1016/j.compositesa.2019.04.011
Received 26 June 2018; Received in revised form 1 April 2019; Accepted 9 April 2019
Available online 13 April 2019
1359-835X/

a 3D model. As mentioned by Xia et al. [17], the shear-lag model yields an accurate prediction of the stress distribution around fiber break points; however, its computational cost is known to be more expensive than that of the above-mentioned LGF approach. Therefore, to improve computational efficiency, Okabe et al. [18] proposed a novel approach referred to as the spring element model, which couples the shear-lag model with analytical stress recovery and enables the analysis of the stress state of the composites, with the exception of the stress recovery region. Tavares et al. [19] recently developed the spring element model to consider a random fiber packing and hybrid fiber structure. Moreover, improved computer techniques have enriched the understanding of the failure processes of UD composites [20–22].

According to previous reports, the failure processes of UD composites can be explained as follows: the load perturbation resulting from a fiber failure is not uniformly distributed among the surviving fibers because it is more heavily applied to the adjacent fibers. Thus, when one fiber breaks, the load that it is carrying is principally transferred to the surviving neighbors, increasing the amount of stress concentrated on these fibers relative to more distant fibers and increasing the probability of failure at this position. This consequently leads to the formation of clusters of broken fibers, and subsequent failure of the composites. Considering this, although most studies to date have only addressed the load redistribution caused by fiber breakage, several studies that have implemented fragmentation tests have reported that a matrix crack or damage to the matrix originates around a fiber break point. Moreover, although the local stress on fibers adjacent to a broken fiber has been widely recognized as critical to the strength of unidirectional CFRP composites, an adequate method for predicting the strength of these composites — one that considers the stress concentration on the fiber surface resulting from a fiber break in a neighboring fiber — is yet to be developed.

In the last few decades, techniques such as Raman spectroscopy [23–28], polarized-light microscopy [29,30], acoustic emission [31], and synchrotron radiation computed tomography [22,32], have been employed to experimentally investigate the stress concentration in composites with *in-situ* observations of fiber breakage. As an example, Jones et al. [29] directly measured the stress concentration on fibers adjacent to a broken fiber by using a multi-fiber fragmentation technique in which nine individual fibers were arranged parallel to the load axis. The authors reported that the stress concentration tended to increase with the decreased interfiber spacing, and that the fiber-fracture phase transition from the original statistical distribution of strength to possessing areas of concentrated stress occurred at a fiber spacing of eight fiber diameters. Similarly, Van den Heuvel et al. [23] also observed the fiber fragmentation behavior in multi-fiber composites by implementing a Raman spectroscopy technique. They found that the transition occurred at a fiber spacing of nine fiber diameters. These results [23,29] suggest that, for cases in which commercial composites with a small interfiber spacing are implemented, fiber breakage primarily occurs as a consequence of stress concentration, which typically leads to the breakage of the fiber directly adjacent to a fractured fiber; this implies that, the fragmentation patterns in embedded fibers are similar. Furthermore, Van den Heuvel et al. also investigated the strain distribution along the longitudinal axis of fibers [26]; however, the measured stress concentration factor (SCF) was not sufficiently high in inducing successive fiber failure in the neighboring fibers. Based on these results, we have inferred that the area excited by the Raman incident light is inclined at an angle of 90° with respect to the area of stress concentration, as illustrated in Fig. 1. Thus, even if the measured strain is not sufficiently high, the significant (localized) stress concentration is expected to generate on the surface of an intact fiber near a fiber break point. This has already been recognized and investigated by Xia et al. [17] and Swolfs et al. [33]. Watanabe et al. [34] recently conducted fundamental research to determine the surface SCF by performing double-fiber fragmentation tests, and subsequently compared the results to the corresponding results of a spring element model simulation, which considered the added concentrated stress on the fiber surface adjacent to a broken fiber. Moreover, they demonstrated that applying the acquired SCF to a spring element model simulation yields results that are consistent with experimentally obtained strengths of unidirectional CFRP composites. The fact that fragmentation testing yields different stress concentrations for different types of matrix materials implies that the strengths of composites are dependent on the matrix materials. However, to our knowledge, no report has presented the tensile strength to be predicted from the SCF obtained from fragmentation composites made with different matrix materials. Moreover, no comparison or verification has been offered using actual composite materials. Furthermore, the procedure for determining the surface stress concentration remains tentative.

In this study, we considered the surface stress concentration on fibers caused by a fracture site in an adjacent fiber into our prediction of the ultimate tensile strengths of unidirectional CFRP composites. The stress concentrated on the fiber surface was determined by performing multi-fiber fragmentation tests in combination with a spring element model simulation. We defined the coordinated fracture to quantitatively evaluate the SCFs. The acquired SCFs were subsequently applied to obtain the tensile strength prediction of unidirectional CFRP composites. The composites were fabricated with T1100G carbon fiber and four types of epoxy materials with different mechanical characteristics. We tested these materials to validate the proposed prediction method. The size scaling results obtained in conjunction with the results from the spring element model simulation were reasonably consistent with the experimental data on the strengths of the four types of unidirectional CFRP composites used herein. A scenario on the origin of stress concentrations generated on an intact fiber surface is investigated through a numerical analysis based on the finite element method.

2. Experimental method

2.1. Sample preparation and mechanical characterization

High-strength, polyacrylonitrile (PAN)-based carbon fiber (TORAYCA™ T1100G) and four types of bisphenol-A epoxy resin materials were used to prepare multi-fiber and UD composites. Table 1 presents a summary of the physical and mechanical properties of the fiber and the matrix. Note that the tensile-loading experiments performed herein revealed that the four types of epoxy materials exhibited different mechanical characteristics (details on the sample preparation and mechanical evaluation are provided in the Supplementary Material). Thus, the epoxy materials are hereafter referred to as "A-epoxy," "B-epoxy," "C-epoxy," and "D-epoxy," with the order of the names indicating the magnitude of the elastic modulus (lowest to highest).

Most related studies have implemented various statistical models to describe the statistical distribution of fiber strength, such as the unimodal Weibull distribution, Weibull of Weibull distribution, bimodal Weibull distribution, lognormal distribution, and Gaussian distribution. We chose to apply the bimodal Weibull distribution as the statistical distribution of fiber strength, based on the report by Watanabe et al. [34]. Table 2 summarizes the parameters used to construct the bimodal Weibull distribution for the T1100G carbon fiber used herein (the detailed procedures for determining the bimodal Weibull parameters will be discussed in Section 2.2). Two different types of PAN-based carbon fibers reported by Watanabe et al. [30,34] are also indicated in Table 2. Note that different types of PAN-based carbon fibers possess a different statistical distribution of strength.

Multi-fiber fragmentation specimens were prepared by positioning two to four fibers parallel to the loading direction, implementing an interfiber spacing of approximately 3.5–20.0 μm (i.e., approximately one-half to four fiber diameters). After adjusting the interfiber spacing, the fibers were translated and glued onto two pieces of plastic tape with an interspatial distance of approximately 80 mm, then positioned in a

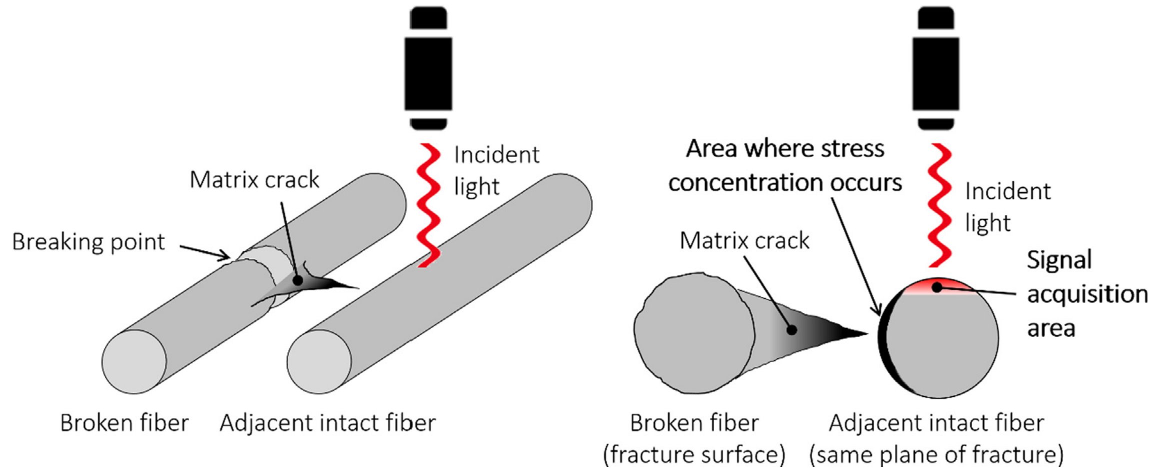

Fig. 1. Schematic showing the relationship between the stress concentration area and the area excited by Raman incident light. (For interpretation of the references to colour in this figure legend, the reader is referred to the web version of this article.)

Table 1
Physical and mechanical properties of the T1100G carbon fiber and the four types of epoxy materials: Young's modulus (E), tensile strength (σ), Poisson's ratio (ν), failure strain (ε), and diameter (D). The average value is given, and the range is indicated in parentheses.

	E (GPa)	σ (MPa)	ν (–)	ε (%)	D (μm)
Carbon fiber	324	7000	–	–	5.4
A-epoxy	3.10	94.0	0.34	6.2	n/a
	(2.82–3.47)	(78.3–103.4)	(0.32–0.38)	(4.1–7.8)	
B-epoxy	3.26	97.0	0.34	8.1	n/a
	(3.18–3.45)	(95.5–98.4)	(0.33–0.34)	(7.8–8.4)	
C-epoxy	3.33	101.0	0.34	6.6	n/a
	(3.14–3.48)	(96.3–103.5)	(0.39–0.36)	(5.6–7.3)	
D-epoxy	3.80	102.9	0.34	7.5	n/a
	(3.72–3.93)	(101.3–105.2)	(0.32–0.35)	(7.3–7.7)	

Table 2
Bimodal Weibull parameters of the T1100G carbon fiber and two different types of PAN-based carbon fibers (i.e., T800S and T700S).

	σ_{01}	m_1	σ_{02}	m_2	Source
T1100G	7.7	4.5	9.1	13.0	This study
T800S	6.9	4.1	8.3	13.0	Refs. [30,34]
T700S	5.2	4.8	6.1	12.0	Refs. [30,34]

glass mold, such that the embedded depth of the fibers was approximately 60 μm from the surface of the specimen. Subsequently, a preheated and degassed epoxy resin was poured into the preheated glass mold in which the fibers were bonded. Finally, the specimens were cured in an air oven at 160 °C for 5 h prior to post-curing at 180 °C for 2 h. The specimens were cooled in the oven to room temperature before being cut into 74 mm (length) × 26 mm (width) samples using a wheel saw (Metkon, METACUT 251).

Multi-fiber fragmentation tests were performed to facilitate the derivation of a quantitative description of fiber failure processes by using a polarized-light microscope (OLYMPUS, BX60) equipped with a custom-made four-point bending machine. The inner and outer span lengths were 18 mm and 50 mm, respectively. A strain gauge (KYOWA, KFG-2-120-C1-11) was attached on the surface of the multi-fiber composites subjected to tensile loading to monitor the tensile strain applied to the fibers. The strain was increased in 0.1% steps until a maximum of 5.0% tensile strain was achieved and held constant during the observation of both the number and positions of the broken fibers. The number of broken fibers observed under the pure bending conditions (i.e., at the central part of the specimen (= 10 mm in length)), was counted using the polarized-light microscope. The strain applied to the fiber ε_f was calculated as follows:

$$\varepsilon_f = \varepsilon_c \times \frac{2.0}{\kappa} \times \left(\frac{t-2d}{t}\right) - \varepsilon_f^r, \tag{1}$$

where ε_c is the measured composite strain, κ is the strain gauge factor (= 2.13), t is the thickness of the multi-fiber composites (= ~2 mm), d is the embedded fiber depth of the fibers (= ~60 μm), and ε_f^r is the indirectly applied strain originating from the included residual compressive strain on the fiber caused by the thermal expansion mismatch between the fiber and the matrix, as determined via Raman spectrum analysis. Both t and d were measured prior to fragmentation testing.

The tensile strengths of the prepared unidirectional CFRP composites were measured to validate the accuracy of the tensile strength predicted by a spring element model derived based on the multi-fiber fragmentation test results. The composites were prepared via conventional vacuum bagging and autoclave laminating technique to produce the laminate structure of $[0_6]$. The maximum applied pressure during processing was approximately 0.6 MPa. The respective curing and post-curing temperatures and durations were identical to those employed in the multi-fragmentation specimen preparation. The fiber volume fraction and the bulk density of the resultant composites were 57% and 1.79 Mg/m^3, respectively. The tensile strength of each of the composites, in the form of a 12.7 mm (width) × 1.1 mm (thickness) × 230 mm (length) test specimen, was measured via a tensile-loading experiment under ambient conditions. The gauge length and the crosshead speed for the tensile tests were 127 mm and 21.2 μm/s (1.27 mm/min), respectively. A strain gauge was used to measure the longitudinal strain of one side of the specimen. Five samples for the four types of unidirectional CFRP composites were measured. The ranges of the measured properties, in addition to the averaged values, are reported in subsequent sections.

2.2. Model preparation

Monte-Carlo methods were implemented in the spring element model simulation to determine the stress concentrated on the surface of the intact fibers surrounding the fiber break points. The spring element model comprises longitudinal and transverse spring elements in a three-dimensional hexagonal arrangement [18,30]. The longitudinal element represents fibers that exclusively carry the tensile load, whereas the transverse element represents the matrix that only sustains the shear load. The stiffnesses of the longitudinal spring element $\boldsymbol{K}_L^e$ and transverse spring element $\boldsymbol{K}_T^e$ are respectively calculated as follows:

$$\boldsymbol{K}_{\mathrm{L}}^{\mathrm{e}} = \pi R^2 \int_0^l \boldsymbol{B}_{\mathrm{L}}^{\mathrm{eT}} E \boldsymbol{B}_{\mathrm{L}}^{\mathrm{e}} \mathrm{d}z, \tag{2}$$

$$\boldsymbol{K}_{\mathrm{T}}^{\mathrm{e}} = \frac{\pi R l}{3} \int_0^l \boldsymbol{B}_{\mathrm{T}}^{\mathrm{eT}} G \boldsymbol{B}_{\mathrm{T}}^{\mathrm{e}} \mathrm{d}r, \tag{3}$$

$$\boldsymbol{B}_{\mathrm{L}}^{\mathrm{e}} = \left[\frac{1}{l} - \frac{1}{l}\right], \tag{4}$$

$$\boldsymbol{B}_{\mathrm{T}}^{\mathrm{e}} = \left[\frac{1}{d} - \frac{1}{d}\right], \tag{5}$$

where L and T represent the longitudinal and transverse directions, respectively, E is the Young's modulus of a fiber, G is the shear modulus of a matrix, R is the radius of a fiber, and l and d are the spring lengths along the longitudinal and transverse directions, respectively. The length of the transverse spring d can be obtained as follows:

$$d = \begin{cases} 0.01 & (\mathrm{f} \le 4) \\ R\left(\sqrt{\frac{2\pi}{\sqrt{3}V_{\mathrm{f}}}} - 2\right) & (\mathrm{f} > 4) \end{cases}, \tag{6}$$

where V_{f} and f are the fiber volume fraction and the number of fibers in the model, respectively. The experimentally observed average interfiber spacing in the multi-fiber fragmentation specimens was approximately 0.01 mm (10 µm). Therefore, d was set to 0.01 to analyze the results of the multi-fiber fragmentation tests performed under the condition that the maximum number of fibers in the model is four. Conversely, a hexagonal close-packed structure was assumed for the analysis of the unidirectional CFRP composites. In spring element models with two to four fibers, the longitudinal spring elements other than fibers are assigned as a matrix; thus, the stiffness of a matrix is implemented in the longitudinal spring elements.

The stress profile of fibers generally varies because of plastic deformation and damage, such as debonding and matrix cracking. The matrix is indirectly modeled in this study; hence, implementing debonding and matrix cracking would be difficult. Therefore, for simplicity, this model considered only the effect of the plastic deformation of the matrix. We considered the situation in which the fiber axial stress within the stress recovery region σ_{s} can be expressed as a linear function of the distance D_{s} from the fiber break point, as is described by the following equation [18]:

$$\sigma_{\mathrm{s}} = \frac{2\tau_{\mathrm{s}} D_{\mathrm{s}}}{R}, \tag{7}$$

where τ_{s} is the interfacial shear stress that is assumed to be constant, which means that the matrix is modeled as a perfectly elastoplastic body. Thus, the equilibrium equation to represent the entire system is expressed as follows:

$$\left[\sum_{e=1}^{N_{\mathrm{f}}-N_{\mathrm{b}}-N_{\mathrm{p}}} \boldsymbol{K}_{\mathrm{L}}^{\mathrm{e}} - \sum_{e=1}^{N_{\mathrm{m}}} \boldsymbol{K}_{\mathrm{T}}^{\mathrm{e}}\right]\boldsymbol{u} + \sum_{e=1}^{N_{\mathrm{p}}} \pi R^2 \int_0^l \boldsymbol{B}_{\mathrm{L}}^{\mathrm{e}^{\mathrm{T}}} \sigma_{\mathrm{s}} \mathrm{d}z = \boldsymbol{f}, \tag{8}$$

where N_{f} and N_{m} are the number of fiber and matrix elements, respectively, N_{b} is the number of broken fibers, and N_{p} is the number of fiber elements in the plastic deformation regions.

We considered herein the situation in which the fiber failure is assumed to occur at the fiber surface, based on the fact that almost all fibers were broken by surface flaws [34]. The fiber breakage probability $P_{\mathrm{f}}(\sigma)$ under the condition that the fiber is subjected to stress σ at the surface area S_{f} (=$2\pi RL_{\mathrm{f}}$) is expressed as follows:

$$P_{\mathrm{f}}(\sigma) = 1 - \exp\left\{-\frac{S_{\mathrm{f}}}{S_{\mathrm{f},0}}\left(\frac{\sigma}{\sigma_{01}}\right)^{m_1} - \frac{S_{\mathrm{f}}}{S_{\mathrm{f},0}}\left(\frac{\sigma}{\sigma_{02}}\right)^{m_2}\right\} \tag{9}$$

where L_{f} is the gauge length, $S_{\mathrm{f},0}$ (=$2\pi RL_{\mathrm{f},0}$) is the representative surface area of the fiber ($L_{\mathrm{f},0}$ = 10 mm), σ_{01} and σ_{02} are the Weibull scale parameters, and m_1 and m_2 are the Weibull shape parameters. The parameters in the first term within the brackets, σ_{01} and m_1, were obtained through single-fiber tensile tests under the representative length ($L_{\mathrm{f},0}$) of 10 mm and gauge lengths of 10, 25, and 50 mm (the detailed procedures for determining σ_{01} and m_1 are explained in the Supplementary Material). Fig. S2 in the Supplementary Material shows Weibull plots of the T1100G carbon fiber determined using Eq. (S1). The intercept (σ_{01} = 7.7) and the slope (m_1 = 4.5) were determined by applying a least-squares technique to the acquired Weibull plots. Fiber breaking behavior obtained from single-fiber fragmentation tests is shown in Fig. 2. It is observed that fiber break behavior calculated by implementing unimodal Weibull parameters (indicated by the red dashed line) is not consistent with the experimentally obtained data. Therefore, the second term parameters, σ_{02} and m_2, were determined by using the elastoplastic shear-lag model to apply a curve-fitting scheme to the experimental data [35]. The fitting results and resultant parameters are presented in Fig. 2 and Table 2, respectively.

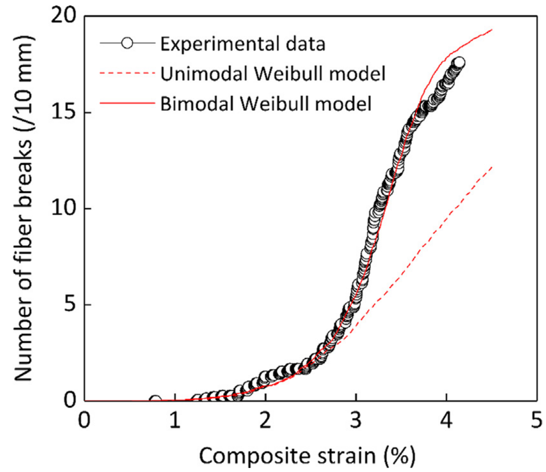

Fig. 2. Fiber breaking behavior obtained from single-fiber fragmentation tests. The behaviors calculated using both the unimodal Weibull parameters and the bimodal Weibull parameters are indicated. (For interpretation of the references to colour in this figure legend, the reader is referred to the web version of this article.)

Fibers are hexagonally arranged in the model; thus, the fiber surface can be divided into six segments, as illustrated in Fig. 3. The surface SCF of the i-th fiber segment adjacent to a broken fiber at the plane of fracture was considered by assuming that it was α_{i} times the average stress on the surface of an adjacent fiber. This is given as follows:

$$\alpha_{\mathrm{i}} = 1 + \gamma_{\mathrm{i}}\left(1 - \frac{D_{\mathrm{s}}}{l_{\mathrm{s}}}\right). \tag{10}$$

$$\gamma_{\mathrm{i}} = \begin{cases} 0 & \text{(a fiber segment facing a neighboring intact fiber)} \\ \alpha - 1 & \text{(a fiber segment facing a neighboring broken fiber)} \end{cases} \tag{11}$$

where α is the SCF of a fiber adjacent to a broken fiber in the same plane, D_{s} is the distance from the break point, and l_{s} is the stress recovery length. Thus, considering the contribution of stress concentration on an intact fiber surface, the fiber breakage probability $P_{\mathrm{f,i}}(\sigma)$ can be rewritten as follows:

$$P_{\mathrm{f,i}}(\sigma) = 1 - \exp\left\{-\frac{S_{\mathrm{f,i}}}{S_{\mathrm{f},0}}\left(\frac{\alpha_{\mathrm{i}}\sigma}{\sigma_{01}}\right)^{m_1} - \frac{S_{\mathrm{f,i}}}{S_{\mathrm{f},0}}\left(\frac{\alpha_{\mathrm{i}}\sigma}{\sigma_{02}}\right)^{m_2}\right\}, \tag{12}$$

where $S_{\mathrm{f,i}}$ is the i-th fiber segment of surface area ($S_{\mathrm{f,i}} = \pi RL_{\mathrm{f},0}/3$). As mentioned earlier, the spring element model does not directly represent the matrix aside from the shear load. Therefore, the additional stress concentration is added in an ad-hoc manner to capture the experimentally measured correlations in fiber breaks.

The strength of the n-th fiber segment is determined by choosing a random number R_{n} ranging from 0 to 1 and solving equation $R_{\mathrm{n}} = P_{\mathrm{f,n}}(\sigma_{\mathrm{n}})$. The longitudinal element was removed from the model

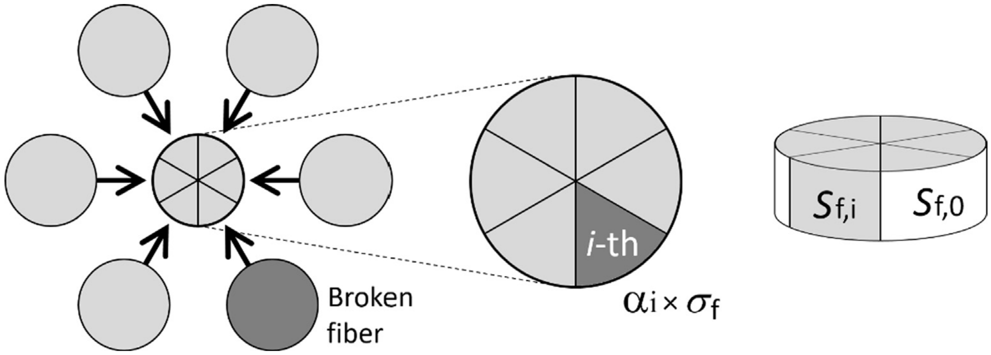

Fig. 3. Definition of the stress concentration on the surface of the *i*-th fiber segment.

when the stress applied to a fiber at the n-th fiber segment achieved the statistical distribution of the strength of the fiber σ_n.

2.3. Determination of the stress concentration factor

The SCFs α on the surface of an intact fiber were determined by employing the spring element model to investigate the α value, with the aim of ensuring that it was equivalent to the percentage of the coordinated fracture, which is defined as a failure occurring at the elements neighboring a broken element in the horizontal plane of the broken fiber element, that was determined via multi-fiber fiber fragmentation testing. Thus, the two to four longitudinal spring elements in the center of the spring element model were assigned to the fibers, and the remaining elements were assigned to the matrix. The fiber elements measuring 10 mm in length were divided into 2000 segments (i.e., the unit length of the fiber element was 5 µm). A coordinated fracture was defined as a failure that occurred at neighboring elements next to a broken element in the same horizontal plane with respect to the broken fiber element. Note that we previously analyzed how the fiber break point is changed by varying α from 1.0 to 2.0 using a double-fiber composite model [30]. Under the condition that α is 1.0, the fiber break positions of two fibers were observed to randomly distribute along the fiber axis direction. By contrast, the simulation results obtained considering an additional stress concentration of $\alpha = 2.0$ agreed well with the fiber break behavior obtained from the experiments.

2.4. Tensile strength determination of unidirectional CFRP composites

The tensile strengths of the unidirectional CFRP composites were predicted via the spring element model. The bimodal Weibull distribution was applied as the statistical distribution of fiber strength. The model comprised 1024 fibers measuring 3 mm in length that were divided into 300 segments. The stress concentration was applied to the surface of the intact fibers according to Eq. (10). The tensile strength is defined as the applied maximum composite stress, and the final failure is assumed to be in progress once the average fiber stress decreases to 90% of the maximum fiber stress (as shown in Supplementary Fig. S3, maximum composite stress does not vary when the criterion of the final failure is changed to 70%, 80%, or 90%). Prior to comparing the simulated results to the experimental data, the simulated strengths were subjected to size scaling, as follows [36]:

$$nL = -n_s L_s / \ln(1 - F_s(\tilde{\sigma}_n)), \tag{13}$$

where n_s is the number of the fibers ($n_s = 1024$), L_s is the length of the composite ($L_s = 3$ mm), $F_s(\tilde{\sigma}_n)$ is the cumulative probability of failure at a given strength as determined by 100 spring element model simulation runs, and nL is the size at which the characteristic strength is achieved.

3. Results and discussion

3.1. Mechanical evaluation of unidirectional CFRP composites

First, we prepared unidirectional CFRP composites consisting of the four types of matrix polymers, and subsequently employed tensile-loading tests to investigate their mechanical properties along the direction of the fiber axis. Fig. 4 and Table 3 summarize the representative stress-strain behavior and summary of the measured mechanical properties, respectively. Note that all composites tested in this study experienced catastrophic failure after reaching a maximum load, exhibiting a stress-strain relationship that is typically observed in conventional unidirectional CFRP composites. As presented in Table 3, no significant difference was observed between the Young's modulus values, whereas for example the composite fabricated with the D-epoxy demonstrated strength enhanced by a factor of approximately 1.2 compared to the composite made with the A-epoxy.

3.2. Tensile strength prediction of B-epoxy matrix composites

As previously mentioned, the fibers surrounding a broken fiber were subjected to increased stress concentration, which increased the probability of failure. Therefore, the understanding of the failure phenomena of such fiber is a prerequisite for the tensile strength prediction of unidirectional CFRP composites. First, we investigated the influence of interfiber spacing on the failure phenomena of the fibers by performing a double-fiber fragmentation test. For this test, the B-epoxy material was used in the specimen preparation. Fig. 5 illustrates the birefringence patterns at the fiber break points in the double-fiber fragmentation composites that varied by interfiber spacing. The images

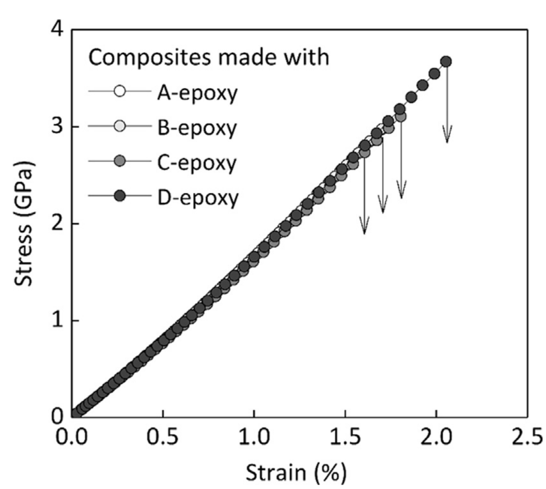

Fig. 4. Representative stress-strain curves for the four types of unidirectional CFRP composites.

Table 3
Measured properties for the four types of unidirectional CFRP composites. Shown are the Young's modulus, tensile strength, and failure strain along the direction of the fiber axis.

	Young's modulus (GPa)	Tensile strength (GPa)	Failure strain (%)
A-epoxy matrix composite	179 (178–180)	3.12 (2.95–3.22)	1.60 (1.51–1.65)
B-epoxy matrix composite	175 (169–179)	3.17 (3.05–3.32)	1.65 (1.59–1.74)
C-epoxy matrix composite	171 (166–175)	3.26 (3.08–3.35)	1.73 (1.67–1.83)
D-epoxy matrix composite	174 (172–177)	3.85 (3.74–3.97)	1.98 (1.93–2.01)

were acquired following an approximately 5.0% alleviation of the composite strain. The illustrations above each of the birefringence patterns demonstrate the positional dependency of neighboring fibers with respect to the fiber break point. 0° indicates a perfect alignment of the fracture site. Irrespective of the interfiber spacing, fiber breakage resulted in matrix crack initiation. Moreover, a large number of fiber failures occurred at similar positions (i.e., at small angles), indicating that the stress concentration caused by fiber fracture was sufficiently high to cause the adjacent fiber to fracture, which nullifies the influence of random distributed flaws along the fiber on the fiber strength. As a fiber-fiber interaction criterion, fiber fractures that occurred at an angle within 0° to 45° are defined as coordinated fractures based on the nature of elastoplastic polymer material fracture phenomena [37]. The percentages of coordinate fractures occurring in double-fiber composites with interfiber spacings of 3.6 µm, 9.9 µm, and 20.0 µm were 73%, 57%, and 60%, respectively. Even though some variation was observed for the percentages of coordinate fractures, the measured percentages appeared to be higher than those observed for fiber failure that were governed by the statistical strength distribution of fibers [23]. This result indicates that for an interfiber spacing of one-half to four fiber diameters, the failure process of the fiber was predominantly governed by the fiber–fiber interactions. Note that debonding was not apparent around the fiber break points in any specimen, suggesting that the composites prepared herein exhibited good interfacial connectivity.

Next, the fiber fracture behavior of the multi-fiber fragmentation composites consisting of up to four fibers was investigated to quantitatively determine the surface SCFs. As shown in Fig. 6, the polarized-light microscopy investigation revealed that matrix cracks and the coordination of fractures in adjacent fibers were observed in multi-fiber fragmentation composites, regardless of the number of fibers. Fig. 7 shows the dependence of the number of fiber breaks in a primary fiber on the percentage of coordinated fractures, with the primary fiber being a fiber with a larger number of breaks. The percentage of coordinated fracture in the double-fiber composites tended to increase as the number of fibers was increased. Figs. 5 and 6 depict that being positioned along the same plane of a fracture does not necessarily mean that the fiber will fracture; thus, the reduction in the percentage of coordinated fractures may be attributable to the fact that coordinated fractures are less likely to occur when the number of fibers is high. At 3.2% fiber strain (i.e., ε_f calculated via Eq. (1) for a composite strain ε_c of 5.0%), the percentages of coordinated fractures (and standard deviation) in the double-, triple-, and quadruple-fiber composites were 48.3% (± 14.1%), 33.3% (± 17.8%), and 15.8% (± 5.8%), respectively. Additionally, the number of fibers and interfiber spacing were not observed to yield any effect on the fracture onset strain (i.e., the strain at which the first fiber failure was generated).

A quantitative determination of the SCFs α on the surface of an intact fiber near a fiber break point was achieved by implementing the spring element model to investigate the value of α. Fig. 8 illustrates the

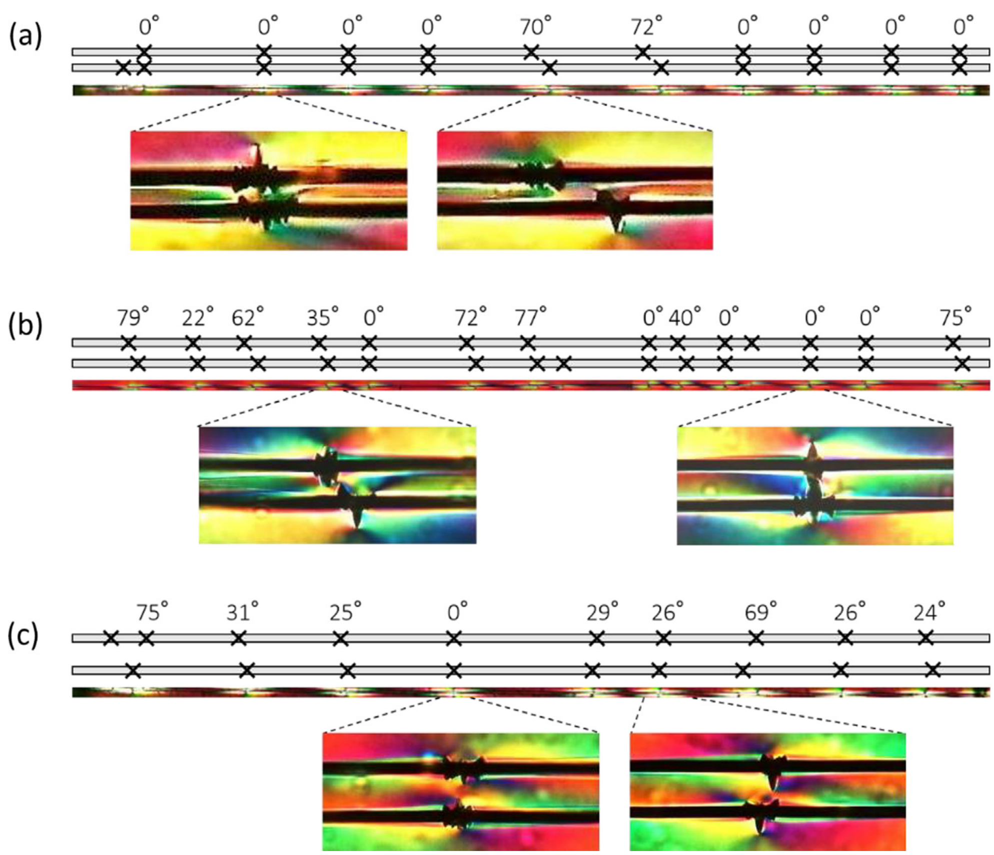

Fig. 5. Birefringence patterns in the double-fiber fragmentation composites with an interfiber spacing of (a) 3.6 µm, (b) 9.9 µm, and (c) 20.0 µm. (For interpretation of the references to colour in this figure legend, the reader is referred to the web version of this article.)

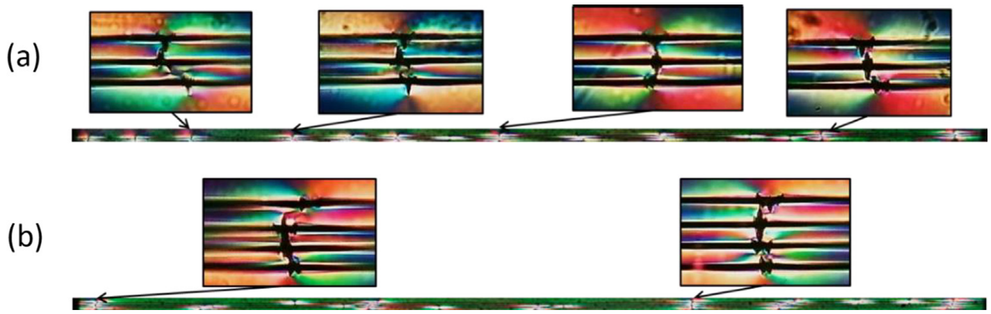

Fig. 6. Birefringence patterns in the (a) triple-fiber fragmentation composite and (b) quadruple-fiber fragmentation composite. The matrix cracks and coordination of fractures are observed for the multi-fiber fragmentation composites with interfiber spacing ranging from one-half to four fiber diameters. (For interpretation of the references to colour in this figure legend, the reader is referred to the web version of this article.)

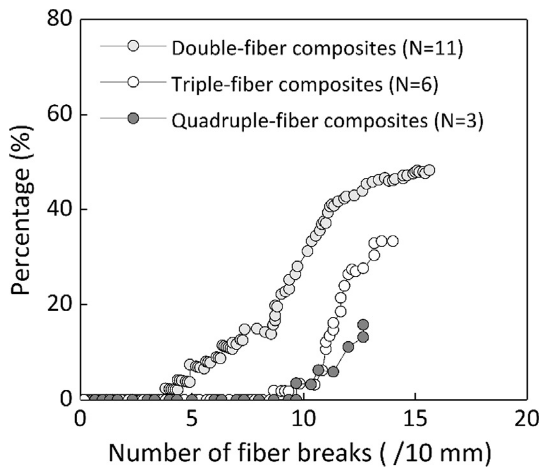

Fig. 7. Effects of the number of fiber breaks in primary fibers on the percentage of coordinated fractures.

relationship between the SCF and the percentage of coordinated fractures for each fragmentation composite, which was determined by systematically sweeping α in the spring element model simulation. The simulation results showed that the percentage of coordinated fractures increased in response to an increased SCF, but decreased with an increase in the number of fibers. Upon comparing the simulated percentages of coordinated fractures to the corresponding experimental observations, the SCF on the surface of an intact fiber was determined to be approximately 2.0. Moreover, the number of fibers did not significantly affect the surface SCF, indicating that for the composites fabricated with B-epoxy, the concentrated stress acting on the fiber surface was twice as much as the fiber stress with no additional surface stress concentration.

As previously mentioned, stress concentration was considered in the prediction of the tensile strength of the unidirectional CFRP composites fabricated with the B-epoxy matrix. Fig. 9 depicts the fiber fracture behaviors on the final failure planes simulated via the spring element model. We defined the plane, including the most fiber breaks, as the final failure plane. A stress ratio of less than 1 in Fig. 9 indicates that the fiber failure occurred near the final failure plane, while a stress ratio of 0 illustrates that the fiber failure occurred in the final failure plane. In the case of no additional stress concentration condition (i.e., $\alpha = 1.0$), the fiber failure was clearly randomly distributed across the plane. This phenomenon is consistent with the statistical distribution of fiber strength. In contrast, additional concentrated stress encourages the formation of broken fiber clusters, which results in relatively premature fracturing. Fig. 10 illustrates a comparison of the experimental and simulated results for the unidirectional T1100G carbon fiber/B-epoxy composites. In this figure, the circles represent the size scaled strength results calculated according to Eq. (13), whereas the cross symbols denote the experimentally obtained tensile strengths of these composites, which ranged from 3.05 to 3.32 GPa (mean: 3.17 GPa). The simulated data obtained without consideration of added concentrated

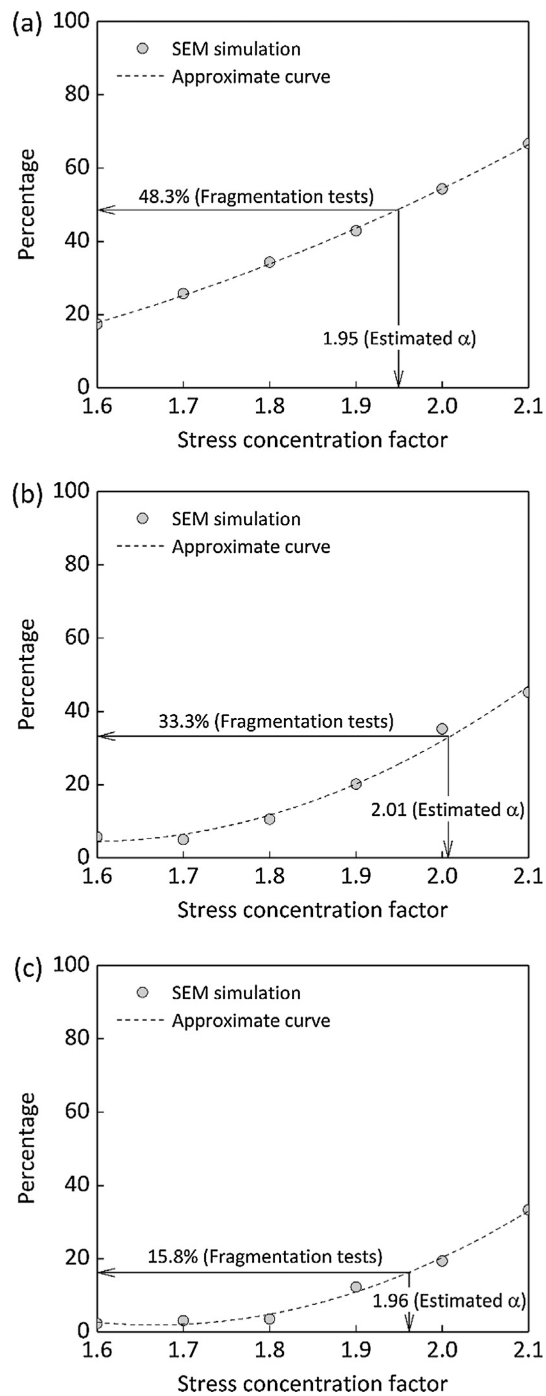

Fig. 8. Relationship between the SCFs and the percentage of coordinated fractures for the (a) double-, (b) triple-, and (c) quadruple-fiber fragmentation composites.

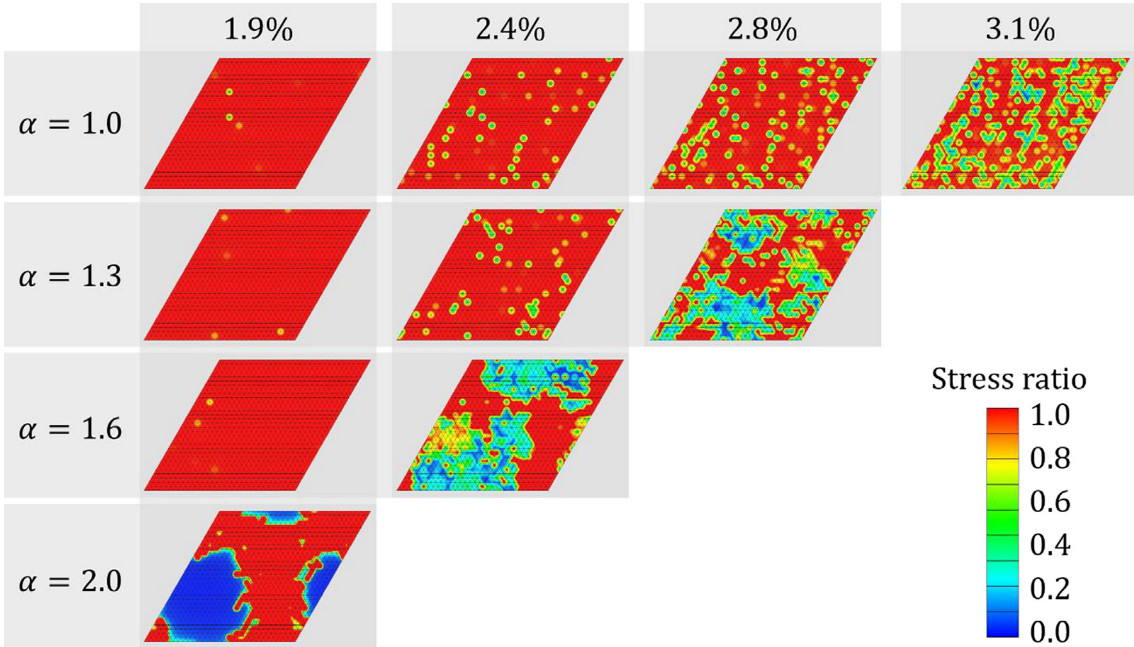

Fig. 9. Distribution of stress in the axial direction on the final failure planes. (For interpretation of the references to colour in this figure legend, the reader is referred to the web version of this article.)

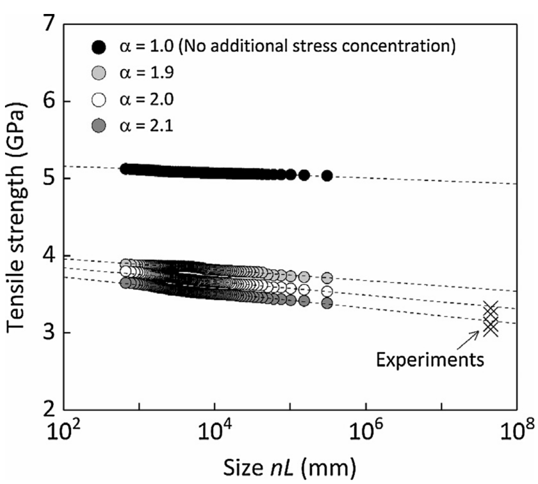

Fig. 10. Experimental and simulated results for the unidirectional T1100G/B-epoxy composites.

stress were incongruent with the experimental data, whereas the predictions incorporating an SCF of 2.0 were reasonably consistent with the experimental data. Furthermore, although the prediction with $\alpha = 2.1$ seemed to yield a better tensile strength prediction than with $\alpha = 2.0$, we conclude that the prediction method proposed herein yields a reasonably accurate tensile strength prediction when the matrix crack-induced surface stress concentration of fibers is appropriately considered.

Previously, Okabe et al. [36] predicted the tensile strength of unidirectional CFRP composites made with T800H carbon fiber, and the result analyzed by the 3D shear-lag model provided the upper limit of the experimental value. However, the strength of the T800H carbon fiber used to predict the tensile strength of the unidirectional CFRP composite was lower than that specified in the supplier's catalog data. In addition, the validity of the strength data is unclear, because these data have not been compared against the results of the single-fiber composite tests discussed in the study; this indicates a need for re-examination of the tensile strength prediction processes reported in [36].

3.3. Application to different types of composites

We applied the above-mentioned strength prediction method to the unidirectional CFRP composites made with the "A-epoxy," "C-epoxy," and "D-epoxy." The SCF on the surface of intact fibers was acquired via double-fiber fragmentation testing considering the fact that for the B-epoxy matrix composites, the number of fibers did not influence the SCFs (Fig. 8). Fig. S4 in the Supplementary Material illustrates the results of implementing SCF determination obtained via double-fiber fragmentation testing and the spring element model simulation. The SCFs were calculated as approximately 2.15 for the A-epoxy, 1.93 for the C-epoxy, and 1.75 for the D-epoxy. A comparison of the results presented in Fig. 8 and Fig. S5 revealed clear differences among them.

Thus, surface SCFs were implemented to predict the tensile strength of the three types of the unidirectional CFRP composites. Fig. 11 presents a comparison of the experimental and simulated results. In one example, the experimentally obtained tensile strengths of the D-epoxy

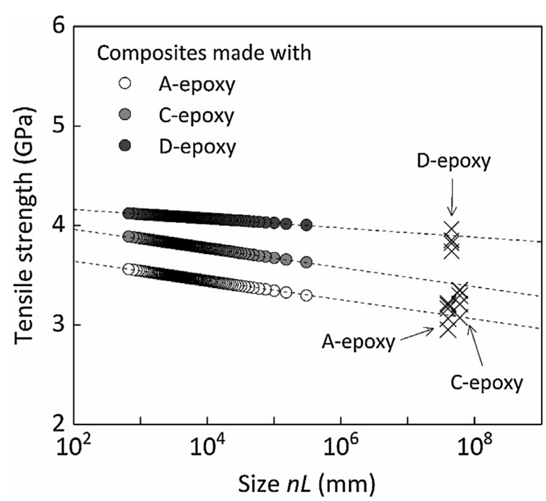

Fig. 11. Experimental and simulated results for the three types of unidirectional CFRP composites. The cross symbols indicate the experimentally obtained tensile strengths of these composites.

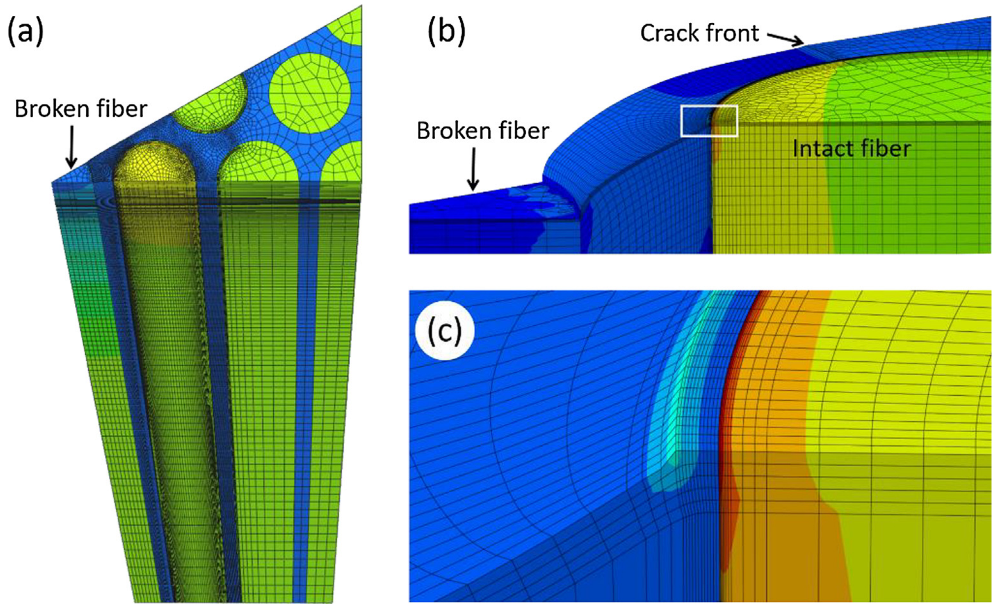

Fig. 12. (a) Schematic representation of the one-twelfth of the composite model. (b) Contour image of normal stress in the fiber axial direction at the 2.0% strain condition. (c) Enlarged image, taken from the white square area in image (b). (For interpretation of the references to colour in this figure legend, the reader is referred to the web version of this article.)

matrix composites ranged from 3.74 to 3.97 GPa (mean: 3.85 GPa), and are denoted by a cross symbol in the figure. The estimated tensile strength simulated under the condition of α=1.75 was approximately 3.9 GPa. This value is reasonably consistent with the experimentally obtained tensile strength. Additionally, a cluster formation on the final fracture plane was observed in the composite system (Supplementary Fig. S5). Consequently, the results demonstrate that, even if the mechanical properties of the matrix materials vary, the proposed method can yield a reasonable prediction of the tensile strength of the unidirectional CFRP composites.

The possible mechanism by which the additional stress concentration occurs is not clear; moreover is it unclear why the SCF varies depending on the matrix characteristics. A numerical analysis using the finite element method was conducted to access possible mechanisms by which higher stress is generated on the intact fiber surface adjacent to the fiber break point. In this analysis, a hexagonal fiber arrangement was used, and only one-twelfth of the structure was modeled and analyzed owing to reasons of structural symmetry. The schematic representation of the one-twelfth of the composite model is shown in Fig. 12(a). The fiber and matrix were assumed to be elasto-plastic and elastic materials, respectively. The matrix was assumed to have rehardening characteristics with a modulus of 0.38 GPa, which is 1/10 of the initial slope in the elastic region of the D-epoxy material. Moreover, the plasticity-free layer model of Suo, Shih, and Varias [38], referred to as the SSV model, an elastic layer with a thickness of 50 nm, was imposed around the matrix crack using the same elastic properties as the D-epoxy material. The matrix crack was assumed not to reach the intact fiber surface and there was a 30 nm-thick elastic layer between the crack tip and the intact fiber surface. Due to the elastic region surrounding the matrix crack, the stress singularity is retained. Displacement control is considered in the model, and the maximum applied composite strain is 2.0%. The elastic stiffnesses of the fiber and the D-epoxy materials are listed in Table 4. The elasto-plastic behavior model

Table 4
Elastic stiffness C_{ij} (GPa) and Young's moduli E_{ij} (GPa) of the T1100G carbon fiber [39] and D-epoxy material. The x_3-axis is parallel to the fiber axis direction.

	C_{11}	C_{33}	C_{13}	C_{44}	C_{66}	E_{11}	E_{33}
Fiber	24.8	314.7	22.7	20.5	5.6	17.0	287.9
D-epoxy	5.8		3.0	1.4		3.8	

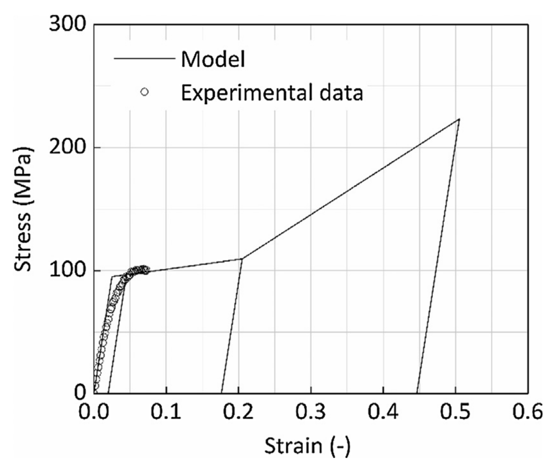

Fig. 13. Elasto-plastic behavior model of the D-epoxy material.

of the D-epoxy material is shown in Fig. 13. Fig. 12(b) and (c) show contour images of normal stress in the fiber axial direction at the 2.0% strain condition.

It was revealed that an SCF of $\alpha = \sim 1.7$, as observed for the D-epoxy matrix composite, was indeed generated on the intact fiber surface by defining the SCF as the ratio of the stress of an outermost surface element of the intact fiber to the stress in an element sufficiently away from the fiber break point. In addition, as shown in Fig. 14, the stress recovery behavior of the broken fiber was reasonably consistent with the behavior obtained from the spring element model simulation under the condition $\alpha = 1$. Fig. 15 shows the positional dependence of the SCF in the circumferential direction of the intact fiber; the SCF decreases rapidly with the increase in the angle, and the SCF decreases almost 1 at about 60°. Note that we previously investigated the SCFs using analytical models that included/excluded SSV and rehardening treatments; the SCFs obtained were less than 1.4 in all the analyses, indicating that no significant increase in the SCFs was observed when excluding the two treatments. We consider that the above-mentioned mechanism is one of the scenarios in which a higher stress is generated on the intact fiber surface. It remains unclear why the SCF varies with the matrix characteristics, and further research is needed to clarify this reason; however, because the degree of SCF depends on the gap between the crack tip and the intact fiber surface, we speculate that the

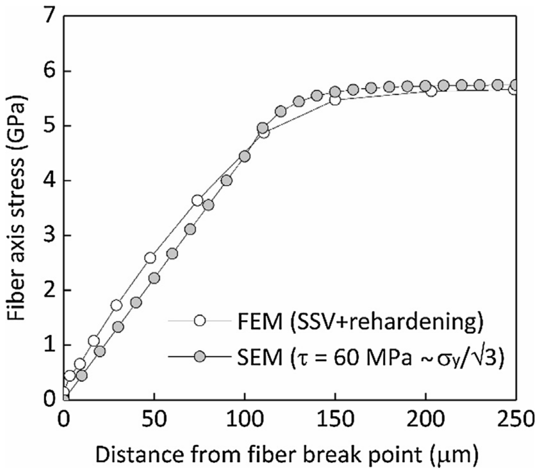

Fig. 14. Comparison of the stress recovery behavior calculated from the finite element simulation and spring element model simulation.

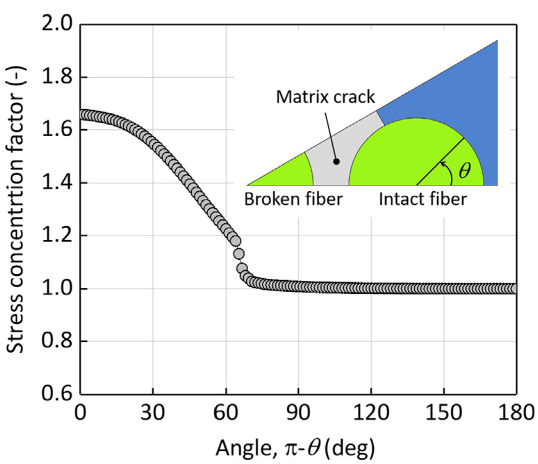

Fig. 15. Positional dependence of the SCF in the circumferential direction of the intact fiber. (For interpretation of the references to colour in this figure legend, the reader is referred to the web version of this article.)

difference in the gap distance was caused by the difference in the mode-I stress intensity factor of the epoxy matrix.

As previously mentioned, improving the accuracy of the tensile strength prediction is central to CFRP composite research. For instance, in certain types of CFRP material [36], our previous model overestimated the ultimate tensile strength compared with the experimentally obtained data, and we could not make a full explanation of its reason. The results indicate that the fact that matrix cracks near the fiber break points increase the amount of stress concentrated on the fiber surface must be considered to obtain a high-accuracy strength prediction. Moreover, the surface SCF must be properly estimated to improve prediction accuracy. Therefore, further work is currently underway to investigate the relationship between the surface SCF and matrix polymer properties, and this will provide useful information to composite researchers. Our findings provide a potential framework that can be implemented to facilitate the development of stronger CFRP composites.

4. Conclusions

Four types of unidirectional CFRP composites with different mechanical characteristics were prepared in this study. The tensile strengths of the fabricated composites were predicted via a numerical simulation based on the results obtained from multi-fiber fragmentation experiments. Furthermore, the primary aim of this study was to explore the effects of matrix polymer properties on the stress concentrated on the fiber surface. Consequently, the multi-fiber fragmentation test results demonstrated that for an interfiber spacing of one-half to four fiber diameters, the failure process of the fiber was predominantly governed by fiber-fiber interactions, irrespective of the matrix polymer properties. We also demonstrated that the degree of stress concentrated on the surface of fibers can be changed by modifying the mechanical properties of the matrix polymer. Additionally, utilizing an epoxy matrix with a higher Young's modulus and increased tensile strength in the composite preparation reduced the SCF from approximately 2.15 to 1.75. We have also shown a numerical scenario on the origin of the stress concentrations that are generated on the intact fiber surface by implementing the SSV model and employing the rehardening characteristics of epoxy materials. Finally, we confirmed that employing the measured SCFs and bimodal Weibull distribution to determine how strength is statistically distributed throughout the fiber yields the predicted strengths of the four types of unidirectional CFRP composites that are reasonably consistent with the experimental data, thereby demonstrating the validity of the proposed prediction method.

Declarations of interest

None.

Acknowledgements

The authors thank Mr. W. Shoichiro of the Department of Aerospace Engineering, Tohoku University, and Dr. R. Higuchi of the Department of Aeronautics and Astronautics, The University of Tokyo, for technical assistance in the FEM analysis. This work was partly supported by Toray Industries, Inc., Japan, the Council for Science, Technology and Innovation (CSTI), Japan, the Cross-ministerial Strategic Innovation Promotion Program (SIP), Japan, and JSPS KAKENHI grant number 18K04721. The authors would like to thank the reviewers for their useful comments and recommendations. The authors would like to acknowledge the vitally important encouragement and support made through the University of Washington-Tohoku University: Academic Open Space (UW-TU: AOS). The authors would like to thank Editage (www.editage.jp) for the English language editing.

Appendix A. Supplementary material

Supplementary data to this article can be found online at https://doi.org/10.1016/j.compositesa.2019.04.011.

References

[1] Cox HL. The elasticity and strength of paper and other fibrous materials. Br J Appl Phys 1952;3(3):72–9.
[2] Rosen BW. Tensile failure of fibrous composites. AIAA J 1964;2(11):1985–91.
[3] Kelly A, Tyson W. Tensile properties of fibre-reinforced metals: copper/tungsten and copper/molybdenum. J Mech Phys Solids 1965;13(6):329–50.
[4] Hedgepeth JM, Van Dyke P. Local stress concentrations in imperfect filamentary composite materials. J Compos Mater 1967;1(3):294–309.
[5] Suemasu H. An analytical study of probabilistic aspect of strength of unidirectional fiber reinforced composite under tensile loads. Trans Japan Soc Compos Mater 1982;8(1/2):29–36.
[6] Suemasu H. Probabilistic aspects of strength of unidirectional fibre-reinforced composites with matrix failure. J Mater Sci 1984;19(2):574–84.
[7] Zweben C. Tensile failure of fibers composites. AIAA J 1968;6(12):2325–31.
[8] Ochiai S, Hojo M. Stress disturbances arising from cut fibre and matrix in unidirectional metal matrix composites calculated by means of a modified shear lag analysis. J Mater Sci 1996;31(14):3861–9.
[9] Ochiai S, Hojo M, Inoue T. Shear-lag simulation of the progress of interfacial debonding in unidirectional composites. Compos Sci Technol 1999;59(1):77–88.
[10] Landis CM, McMeeking RM. A shear-lag model for a broken fiber embedded in a composite with a ductile matrix. Compos Sci Technol 1999;59(3):447–57.
[11] Tanaka M, Ochiai S, Hojo M, Ishikawa T, Kajii S, Matsunaga K, et al. Fracture behavior of unidirectional Si-Ti-C-O fiber-bonded ceramic composite materials. Key Eng Mater 1999;164–165:141–4.
[12] Sastry AM, Phoenix SL. Load redistribution near non-aligned fibre breaks in a two-

dimensional unidirectional composite using break-influence superposition. J Mater Sci Lett 1993;12(20):1596–9.
[13] Beyerlein IJ, Phoenix SL. Stress concentrations around multiple fiber breaks in an elastic matrix with local yielding or debonding using quadratic influence superposition. J Mech Phys Solids 1996;44(12):1997–2036.
[14] Zhou SJ, Curtin WA. Failure of fiber composites: A lattice green function model. Acta Metall Mater 1995;43(8):3093–104.
[15] Landis CM, Beyerlein IJ, McMeeking RM. Micromechanical simulation of the failure of fiber reinforced composites. J Mech Phys Solids 2000;48(3):621–48.
[16] Okabe T, Takeda N, Kamoshida Y, Shimizu M, Curtin WA. A 3D shear-lag model considering micro-damage and statistical strength prediction of unidirectional fiber-reinforced composites. Compos Sci Technol 2001;61(12):1773–87.
[17] Xia Z, Curtin WA, Peters PWM. Multiscale modeling of failure in metal matrix composite. Acta Mater 2001;49(2):273–87.
[18] Okabe T, Sekine H, Ishii K, Nishikawa M, Takeda N. Numerical method for failure simulation of unidirectional fiber-reinforced composites with spring element model. Compos Sci Technol 2005;65(6):921–33.
[19] Tavares RP, Otero F, Turon A, Camanho PP. Effective simulation of the mechanics of longitudinal tensile failure of unidirectional polymer composites. Int J Fract 2017;208(1-2):269–85.
[20] Chou HY, Bunsell AR, Mair G, Thionnet A. Effect of the loading rate on ultimate strength of composites. Application: Pressure vessel slow burst test. Compos Struct 2013;104:144–53.
[21] Thionnet A, Chou HY, Bunsell A. Fiber break processes in unidirectional composites. Compos Pt A-Appl Sci Manuf 2014;65:148–60.
[22] Swolfs Y, Morton H, Scott AE, Gorbatikh L, Reed PAS, Sinclair I, et al. Synchrotron radiation computed tomography for experimental validation of a tensile strength model for unidirectional fibre-reinforced composites. Compos Pt A-Appl Sci Manuf 2015;77:106–13.
[23] Van Den Heuvel PWJ, Van Der Bruggen YJW, Peijs T. Failure phenomena in multi-fibre model composites: Part 1. An experimental investigation into the influence of fibre spacing and fibre-matrix adhesion. Compos Pt A-Appl Sci Manuf 1996;27(9):855–9.
[24] Van Den Heuvel PWJ, Peijs T, Young RJ. Failure phenomena in two-dimensional multi-fibre microcomposites: 2. A Raman spectroscopic study of the influence of inter-fibre spacing on stress concentrations. Compos Sci Technol 1997;57(8):899–911.
[25] Van Den Heuvel PWJ, Peijs T, Young RJ. Failure phenomena in two-dimensional multi-fibre microcomposites - 3. A Raman spectroscopy study of the influence of interfacial debonding on stress concentrations. Compos Sci Technol 1998;58(6):933–44.
[26] Van Den Heuvel PWJ, Wubbolts MK, Young RJ, Peijs T. Failure phenomena in two-dimensional multi-fibre model composites: 5. a finite element study. Compos Pt A-Appl Sci Manuf 1998;29(9–10):1121–35.
[27] Van Den Heuvel PWJ, Peijs T, Young RJ. Failure phenomena in two-dimensional multi-fibre microcomposites. Part 4: A Raman spectroscopic study on the influence of the matrix yield stress on stress concentrations. Compos Pt A-Appl Sci Manuf 2000;31(2):165–71.
[28] Van den Heuvel PWJ, Goutianos S, Young RJ, Peijs T. Failure phenomena in fibre-reinforced composites. Part 6: A finite element study of stress concentrations in unidirectional carbon fibre-reinforced epoxy composites. Compos Sci Technol 2004;64(5):645–56.
[29] Jones KD, DiBenedetto AT. Fiber fracture in hybrid composite systems. Compos Sci Technol 1994;51(1):53–62.
[30] Watanabe J, Tanaka F, Higuchi R, Matsutani H, Okuda H, Okabe T. A study of stress concentrations around fiber breaks in unidirectional CF/epoxy composites using double-fiber fragmentation tests. Adv Compos Mater 2018;27(6):575–87.
[31] Pickering KL, Bader MG, Kimber AC. Damage accumulation during the failure of uniaxial carbon fibre composites. Compos Pt A-Appl Sci Manuf 1998;29(4):435–41.
[32] Scott AE, Mavrogordato M, Wright P, Sinclair I, Spearing SM. In situ fibre fracture measurement in carbon-epoxy laminates using high resolution computed tomography. Compos Sci Technol 2011;71(12):1471–7.
[33] Swolfs Y, McMeeking RM, Verpoest I, Gorbatikh L. Matrix cracks around fibre breaks and their effect on stress redistribution and failure development in unidirectional composites. Compos Sci Technol 2015;108:16–22.
[34] Watanabe J, Tanaka F, Okuda H, Okabe T. Tensile strength distribution of carbon fibers at short gauge lengths. Adv Compos Mater 2014;23(1):535–50.
[35] Okabe T, Takeda N. Elastoplastic shear-lag analysis of single-fiber composites and strength prediction of unidirectional multi-fiber composites. Compos Pt A-Appl Sci Manuf 2002;33(10):1327–35.
[36] Okabe T, Takeda N. Size effect on tensile strength of unidirectional CFRP composites experiment and simulation. Compos Sci Technol 2002;62(15):2053–64.
[37] Huang H, Talreja R. Numerical simulation of matrix micro-cracking in short fiber reinforced polymer composites: Initiation and propagation. Compos Sci Technol 2006;66(15):2743–57.
[38] Suo Z, Shih CF, Varias AG. A theory for cleavage cracking in the presence of plastic flow. Acta Mater 1993;41(5):1551–7.
[39] Tane M, Okuda H, Tanaka F. Nanocomposite microstructures dominating anisotropic elastic modulus in carbon fibers. Acta Mater 2019;166:75–84.